Giant intrinsic circular dichroism of enantiomorphic flat Chern bands and flatband devices

Yinong Zhou,[1] Gurjyot Sethi,[1] Chao Zhang [ORCID],[2] Xiaojuan Ni,[1] and Feng Liu [ORCID][1,*]

[1]*Department of Materials Science and Engineering, University of Utah, Salt Lake City, Utah 84112, USA*
[2]*School of Physics, University of Wollongong, Wollongong, New South Wales 2522, Australia*

Circular dichroism (CD) is generally observed in the optically active chiral molecules that originate from *macroscopic* electric and magnetic dipoles, which is usually quite small. In solid states, the so-called valley CD may arise *microscopically* from interband transitions between two chiral electronic valley bands of nonzero Berry curvatures at a given k point. However, generally, two sets of K and K' valleys coexist in the Brillouin zone with opposite chiral selectivities, so that the net CD is zero for the whole material. Here, we demonstrate a giant CD originating from photoexcitation between two chiral Chern flat bands of opposite Chern numbers, namely, the enantiomorphic flat Chern bands. The dissymmetry factor g of such flat CD can reach the theoretical maximum value of 2 with the optimal spin-orbit coupling strength. Based on first-principles calculations, we identify that the Li intercalated bilayer π-conjugated nickel-bis(dithiolene) hosts a set of yin-yang kagome bands with an estimated large $g = 0.74$ under magnetic field. Furthermore, based on the flat-CD mechanism, we propose two flatband devices of topological photodetectors and circularly polarized lasers.

I. INTRODUCTION

Circular dichroism (CD) is a differential absorption spectrum of left-handed (σ^+) and right-handed (σ^-) circularly polarized light (CPL). It usually originates from the macroscopic chiral degree of freedom of naturally occurring molecular structures [see Fig. 1(a)] [1–3]. However, this conventional CD, with a magnitude proportional to the product of electric and magnetic dipole transition moments, is quite small. Its typical dissymmetry factor g lies in the range of $|g| < 0.2$ [4], one order of magnitude smaller than the theoretical maximum value of 2. To overcome this limitation in nature, artificial chiral metasurface structures were recently fabricated to exhibit a giant CD as large as 0.7 [5].

On the other hand, in solid states, CD can have a *microscopic* origin from the chiral degree of freedom of electron bands, even in achiral crystalline structures. One interesting example is the so-called valley CD in two-dimensional (2D) materials, such as graphene [6–10] and transition-metal dichalcogenides [11–18]. In valleytronics, the valence and conduction bands at a given k point of the valley have opposite Berry curvatures, leading to a strong CD when this valley can be isolated by breaking inversion symmetry [12,19]. However, generally, two sets of K and K' valleys coexist in the Brillouin zone with opposite chiral selectivities [see Fig. 1(b)] so that the overall CD vanishes for the whole material.

In this paper, we demonstrate a giant CD originating from photoexcitation between two enantiomorphic flat Chern bands (FCBs) [Fig. 1(c)]. Recently, it was shown that a unique configuration of enantiomorphic flat bands (FBs) can exist in a diatomic kagome lattice, arising as parts of the two sets of

kagome bands that were termed yin-yang kagome bands resulted from negative and positive lattice hoppings [20]. For the spin-degenerate case, the valence and conduction FBs carry opposite spin Chern numbers (i.e., Z_2 number) in each spin channel to support an interesting excited quantum Hall effect [20], as CPL of a given handedness will excite selectively one spin channel to induce a quantized transverse integer or fractional Hall conductivity. However, the net CD would be zero with opposite CPL absorptions from two spin channels. Instead, considering a ferromagnetic system, time-reversal symmetry breaking gives rise to a pair of enantiomorphic FCBs carrying opposite Chern numbers, as shown in Fig. 1(c). Then photoabsorption between the two FCBs is allowed for a CPL of only one handedness (let's say left handed for spin-up bands) but is forbidden for the other, leading to a giant FCB-originated CD (named flat CD) for the whole material. Furthermore, we identify two real candidate materials to realize the pertinent flat-CD phenomena.

II. TIGHT-BINDING MODEL

We first illustrate the creation of enantiomorphic FCBs in the diatomic kagome lattice and a "phase" diagram of band structures in the parameter space of lattice hopping integrals. As shown in Fig. 2(a), there are two atoms (a dumbbell) on each kagome site. The tight-binding (TB) Hamiltonian can be written as

$$H = t_1 \sum_{\langle ij \rangle \alpha} c_{i\alpha}^\dagger c_{j\alpha} + t_2 \sum_{\langle\langle ij \rangle\rangle \alpha} c_{i\alpha}^\dagger c_{j\alpha} + t_3 \sum_{\langle\langle\langle ij \rangle\rangle\rangle \alpha} c_{i\alpha}^\dagger c_{j\alpha}$$

$$+ i\lambda \sum_{\langle\langle ij \rangle\rangle \alpha\beta} \frac{2}{\sqrt{3}} \left(\hat{r}_{ij}^1 \times \hat{r}_{ij}^2 \right) \cdot \sigma_{\alpha\beta}^z c_{i\alpha}^\dagger c_{j\beta} + \lambda_z \sum_{i\alpha} c_{i\alpha}^\dagger \sigma_\alpha^z c_{i\alpha},$$

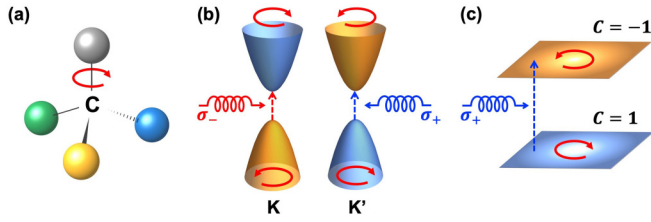*fliu@eng.utah.edu

(1)

125115-1

FIG. 1. Schematic illustration comparing three CD generation mechanisms. (a) The small CD of a chiral molecule originating from macroscopic electric and magnetic dipole transition moments. The red curved arrow represents the structural chirality of the molecule. (b) The valley CD in a 2D material originating from valleytronics with opposite chiral selectivities in the two sets of K and K' valleys in the BZ. The red curved arrows indicate electronic chirality of Berry curvatures in the valley bands. The σ^- (σ^+) CPL is absorbed in the K (K') valley, and the net CD from both valleys is zero. (c) The giant flat CD originating from enantiomorphic FCBs with opposite Chern numbers. The red curved arrows indicate electronic chirality of Berry curvatures in the FCBs. Only the σ^+ CPL is absorbed in the whole system.

where $c_{i\alpha}^\dagger$ ($c_{i\alpha}$) is the electron creation (annihilation) operator on site i of spin α. The first three terms represent the nearest-neighbor (NN) intradumbbell (t_1), 2NN interdumbbell (t_2), and 3NN cross-dumbbell (t_3) hoppings. The fourth term represents spin-orbit coupling (SOC) with a coupling strength λ, with the cross between two 2NN unit vectors $\hat{r}_{ij}^{1,2}$ mimicking an effective magnetic field pointing out from the center of the triangle [Fig. 2(a)]; the coefficient $2/\sqrt{3}$ leads to $2/\sqrt{3}\,(\hat{r}_{ij}^1 \times \hat{r}_{ij}^2) = \pm 1$. σ^z is the Pauli matrix; α and β are spin indices [21]. The fifth term represents the Zeeman splitting with an exchange field strength λ_z. We consider the case of a large Zeeman splitting so that only the spin-up component is taken into account in the following unless otherwise specified.

Figure 2(b) shows the phase diagram of TB band structures in the parameter space of t_2 and t_3, which consists of four different phases: (D, p_{xy}), (K^-, K^-), (K^+, K^-), and a mixed phase. A detailed discussion of these phases and the corresponding band structures (Fig. S1) are presented in the Supplemental Material [22]. Here, we focus on the (K^+, K^-) phase with the desired enantiomorphic FCBs, where K^+
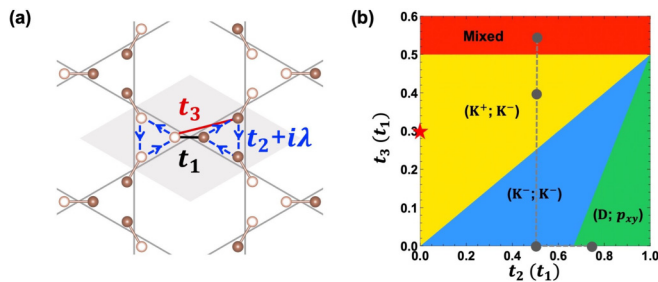

FIG. 2. Lattice and phase diagram of the diatomic kagome lattice. (a) The diatomic kagome lattice structure, where t_1, t_2, and t_3 are hopping integrals and λ represents the SOC strength. (b) Phase diagram of the TB bands as a function of t_2 and t_3 in units of t_1. The red star on the y axis marks the ideal (K^+, K^-) phase we choose for the topological and optical property calculations.
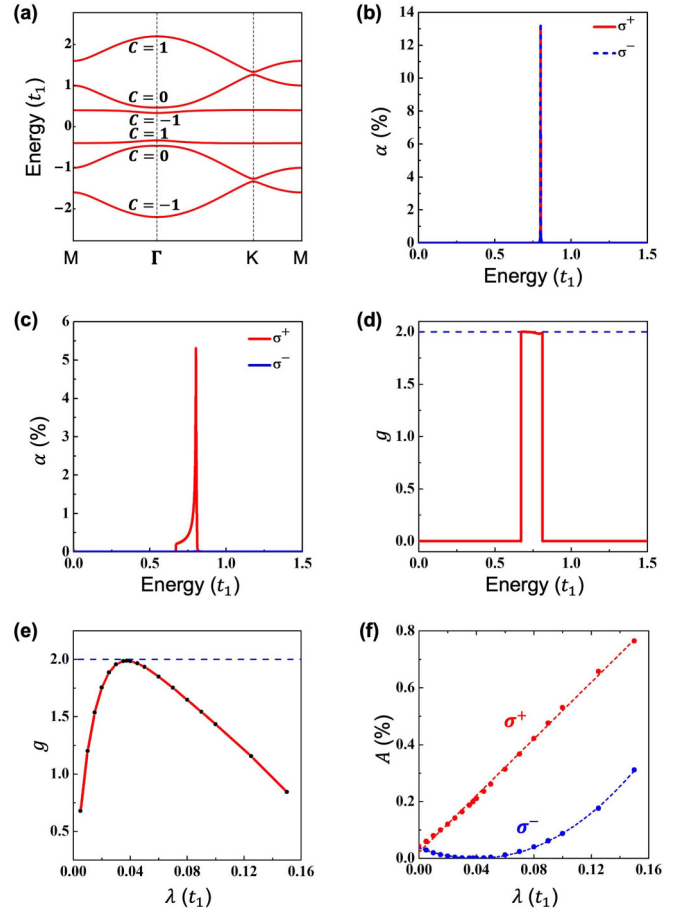

FIG. 3. The topological and optical properties of the (K^+, K^-) phase. (a) The ideal yin-yang kagome band structure and Chern numbers of each band with SOC. (b) The interband optical adsorption coefficient α without SOC, which is the same for the left-handed (σ^+) and right-handed (σ^-) CPL. (c) α with SOC [20]. The FCBs absorb only σ^+ CPL. (d) The dissymmetry factor g calculated from the σ^+ and σ^- absorbance in (c). (e) The g factor as a function of λ for the excitation of yin-yang FCBs. (f) The relationship between the integrated absorbance A and λ for σ^+ and σ^- CPL, respectively.

and K^- denote two subsets of kagome bands resulting from positive and negative lattice hoppings, respectively. To simplify the analysis, we consider an ideal case in the (K^+, K^-) phase by setting $t_2 = 0$. The corresponding lattice hoppings are indicated in Fig. S2(c) [22]. One typical band structure of $t_3 = 0.3t_1$, marked by the red star on the y axis in Fig. 2(b), is shown in Fig. 3(a) with SOC. By integrating the Berry curvatures, the Chern numbers C of two FCBs are calculated to be $C = 1$ and $C = -1$ [23], which we will denote as yin and yang FCBs hereafter for convenience.

III. RESULTS AND DISCUSSION

The contrasting topology of the yin vs yang FCBs leads to a striking optical activity. The calculated optical absorption between the yin and yang FCBs of CPL shows a strong chirality dependence. The interband optical absorption coefficient

$\alpha(\omega)$, where ω is frequency, is given by [9,24,25]

$$\alpha^{\pm}(\omega) = \frac{\alpha_0}{\hbar\omega} \sum_{v,c} \int_{1BZ} |\mathcal{P}_x^{cv}(\boldsymbol{k}) \pm i\mathcal{P}_y^{cv}(\boldsymbol{k})|^2$$

$$\times \frac{\eta}{\pi[(E_c(\boldsymbol{k}) - E_v(\boldsymbol{k}) - \hbar\omega)^2 + \eta^2]} d\boldsymbol{k}, \quad (2)$$

where $\mathcal{P}_x^{cv}(\boldsymbol{k})$ is the electric dipole matrix element $\mathcal{P}_{x,y}^{cv}(\boldsymbol{k}) = \langle\psi_c(\boldsymbol{k})|\vec{\nabla}_{x,y}H(\boldsymbol{k})|\psi_v(\boldsymbol{k})\rangle$. $E_c(\boldsymbol{k})$ and $E_v(\boldsymbol{k})$ and $|\psi_c(\boldsymbol{k})\rangle$ and $|\psi_v(\boldsymbol{k})\rangle$ are eigenvalues and eigenstates of the conduction and valence bands, respectively. η is the full width at half maximum of the Lorentzian, which is the phenomenological relaxation rate for interband transitions. Here, we choose $\eta = 1$ meV. $\alpha_0 = e^2/4\pi\varepsilon_0 c\hbar$, where e and m are the charge and mass of the electron, ε_0 is the vacuum permittivity, and $\hbar$ is the reduced Planck constant.

Without SOC, the optical absorption spectra for σ^+ and σ^- CPL are the same, as shown in Fig. 3(b); both show a sharp δ-function peak at the gap energy between yin and yang FCBs. With the SOC ($\lambda = 0.0375t_1$), the absorbance for σ^+ CPL is much larger than that for σ^- CPL (almost zero), as shown in Fig. 3(c), leading to a giant CD, as quantified by the dissymmetry factor g,

$$g = \frac{\alpha^+ - \alpha^-}{\frac{1}{2}(\alpha^+ + \alpha^-)}. \quad (3)$$

Most significantly, for the chosen parameters, the g value reaches even the maximum theoretical value of 2, as shown in Fig. 3(d).

With SOC, the FCBs become dispersive. Consequently, the g factor, integrated over energy, becomes dependent on the SOC strength, as shown in Fig. 3(e). Specifically, with increasing SOC, g shows a volcanolike curve with a generally large CD ($g > 0.5$). It reaches the maximum value of 2 for $\lambda = 0.0375t_1$ [see also Fig. 3(d)], as mentioned above. This nonlinear relationship between g and λ is caused by the different resonances for the absorption of σ^+ and σ^- CPL, as shown in Fig. 3(f). The integrated absorbance, $A = \int\alpha^{\pm}(\omega)d\omega$, increases linearly with λ for σ^+ CPL but first decreases slightly and then increases as a power law for σ^- CPL.

To better understand such an intriguing CD behavior, we further reveal the k-space distributions of the absorbance for σ^+ and σ^- CPL and the corresponding distributions of the g factor as a function of SOC, as shown in Fig. 4. Without SOC, the absorbances for σ^+ and σ^- CPL are the same, and both originate from concentrated photoexcitation along the Γ_v-M high-symmetry lines (here Γ_v denotes a k point in the vicinity of Γ) while the photoexcitation at Γ and in its vicinity is forbidden [see Figs. 4(a) and 4(e)]. Including SOC, most noticeably, due to the contrasting topology of yin vs yang FCBs, photoexcitation at Γ becomes allowed for the σ^+ CPL but remains forbidden for the σ^- CPL [see Figs. 4(b)–4(d) and 4(f)–4(h)], leading to a giant CD. Specifically, with increasing λ, the absorbance for σ^+ CPL increases monotonically around Γ and along the Γ_v-M line. Meanwhile, the absorbance for σ^- CPL decreases first and then increases along the Γ_v-M line; its intensity is generally an order of magnitude smaller than that for σ^+ CPL and almost vanishes at $\lambda = 0.0375t_1$, which gives rise to the maximum g of 2. The k-resolved g factors are
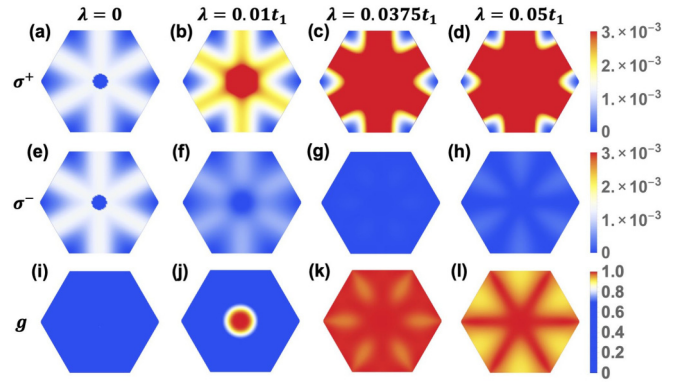

FIG. 4. The interband absorbance distributions. The distributions of (a)–(d) σ^+ and (e)–(h) σ^- CPL in the first BZ for different λ. (i)–(l) The corresponding distributions of g in the first BZ for different λ. (a), (e), and (i) $\lambda = 0$, (b), (f), and (j) $\lambda = 0.01t_1$, (c), (g), and (k) $\lambda = 0.0375t_1$, and (d), (h), and (l) $\lambda = 0.05t_1$.

shown in Figs. 4(i)–4(l). When λ is small, g is predominantly centered at and around the Γ point [Fig. 4(j)]. With increasing λ, g along Γ_v-M is gradually enhanced.

Next, we use group theory to explain the difference between the absorptions with and without SOC at the high-symmetry points. The diatomic kagome lattice has space group $P6/mmm$ (D_{6h}^1) in the Hermann-Mauguin notation. Based on the optical selection rule [26], for a nonzero optical activity, the matrix element $(\psi_c, H'\psi_v)$ must transform as a constant when any or all the symmetry operations are applied, where H' represents the perturbation induced by the CPL. In other words, the matrix element can be calculated by the direct product of the irreducible representations Γ_c for ψ_c, $\Gamma_{H'}$ for H', and Γ_v for ψ_v. If $\Gamma_c \otimes \Gamma_{H'} \otimes \Gamma_v$ contains the fully symmetrical representation Γ_1, the photoexcitation is allowed. The symmetry behavior of H' can be derived by using the *wonderful orthogonality theorem* [26]. For example, at the Γ point, the σ^+/σ^- CPL can be expressed by the complete set of basis functions of the irreducible representations i [27]:

$$\begin{pmatrix} 1 \\ \mp i \\ 0 \end{pmatrix} = \sum_i \frac{l_i}{h} \sum_{R \in D_{6h}} \chi_i(R)\hat{R} \begin{pmatrix} 1 \\ \mp i \\ 0 \end{pmatrix}$$

$$= \begin{cases} \begin{pmatrix} 1 \\ \mp i \\ 0 \end{pmatrix}, & \text{if } i = \Gamma_5^-, \\ 0, & \text{otherwise,} \end{cases} \quad (4)$$

where $(1 \mp i\, 0)^T$ is the Jones vector of the σ^+/σ^- CPL, l_i is the dimension of the irreducible representations i, h is the number of operations in the point group D_{6h} for the Γ point, and χ_i and $\hat{R}$ represent the characters and operations, respectively. Therefore, any CPL mode transforms purely according to the irreducible representation Γ_5^-. Similarly, analysis at the K (point group D_{3h}) and M (point group D_{2h}) points can be performed according to the Γ_6 and $\Gamma_2^- \oplus \Gamma_4^-$ representations, respectively. The relevant irreducible representations for the states of the high-symmetry points are shown in Fig. S3 [22]. The corresponding direct products with and without SOC are shown in Table S1 [22] and are identified in accordance with
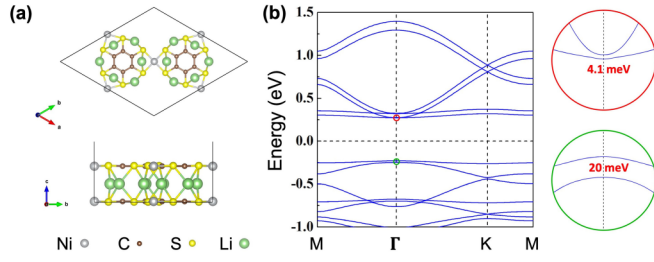
FIG. 5. The atomic and band structures of the Li intercalated bilayer π-conjugated nickel-bis(dithiolene) Li_{12}-$(Ni_3C_{12}S_{12})_2$. (a) The top and side views of the lattice. (b) The band structure with SOC. The red and green circles on the right enclose the zoom-in band structures around the SOC gaps between the conduction (valence) FB and the parabolic band, as indicated by small red and green circles at the Γ point, respectively.

the absorption distributions in Fig. 4. Note that the photoexcitation at the Γ point is forbidden without SOC in Fig. 4 but allowed in Table S1. The reason is that the dispersive bands are also considered in the group theory analysis due to the band degeneracy at the Γ point. With SOC, the band degeneracy is lifted. The total angular momenta are 3/2 and 1/2 for FCBs Γ_9^+ and Γ_7^-, respectively [see Fig. S3(b)], as derived from the double-group theory [28]. As a result, only the σ^+ CPL (satisfying the selection rule of $\Delta J = 3/2 - 1/2 = -1$) can be absorbed with SOC leading to the giant CD.

Furthermore, the SOC-induced absorption around the Γ point can be visually understood by plotting the wave function coefficient in real space, as shown in Figs. S4 and S5 [22]. One notices that the single-orbital diatomic kagome lattice can be viewed as an sp^2 basis in a hexagonal lattice [20]. Without SOC, the orbitals are $|s, \uparrow\rangle$ for Figs. S4(a) and S4(f), $|p_x, \uparrow\rangle$ for Figs. S4(b) and S4(e), and $|p_y, \uparrow\rangle$ for Figs. S4(c) and S4(d). The photoexcitation is forbidden from p to p orbitals. Consequently, the absorbance at the Γ point is zero in Figs. 4(a) and 4(e). In contrast, with SOC, the orbitals become $|s, \uparrow\rangle$ for Figs. S5(a) and S5(f) and $|\pm(p_x \pm ip_y), \uparrow\rangle$ for Figs. S5(b)– S5(d) [29,30]. Consequently, only σ^+ CPL can be absorbed between the two FCBs.

IV. MATERIAL REALIZATION

Now, we identify two candidate materials to realize the above intriguing flat-CD phenomena based on first-principles calculations. The first one is the lithium intercalated bilayer π-conjugated nickel bis(dithiolene) $[Li_{12}$-$(Ni_3C_{12}S_{12})_2]$, whose atomic and electronic band structures are shown in Fig. 5. One can clearly see a set of yin-yang kagome bands, contributed by Ni d orbitals, in Fig. 5(b). With 12 intercalated Li atoms per unit cell, the Fermi level is located right in between the two flat bands. By fitting the TB model Hamiltonian [Eq. (1)] to the designated first-principles yin-yang kagome bands, we estimated its flat-CD effect under magnetic field to have a g value of 0.74, which is unprecedentedly large for any known material. It is important to note that the AB stacked bilayer π-conjugated nickel bis(dithiolene) has been experimentally synthesized [31], and the first-principles calculations show that AA stacking is more stable than AB stacking [32,33]. Here, we use one example configuration of Li intercalation,

where the Li atoms are located at the interface, to illustrate the feasibility of intercalating up to 12 Li atoms per unit cell. The intercalation energy E is found to be negative, -0.31 eV/atom for Li_{12}-$(Ni_3C_{12}S_{12})_2$, calculated as $E = [E(\text{tot}) - E(\text{bilayer}) - nE(\text{Li})]/N$, where $E(\text{tot})$ is the total energy of the intercalated system, $E(\text{bilayer})$ is the energy of pure $(Ni_3C_{12}S_{12})_2$, $E(\text{Li})$ is the energy of a Li atom, n is the number of Li atoms, and N is the total number of atoms. The second one is anilato-based metal-organic frameworks, such as $Cr_2(C_6O_4I_2)_3$, which is found to not only host a set of yin-yang flat bands but also to have a ferromagnetic state which is about degenerate with the antiferromagnetic state and much more stable than the nonmagnetic state (see Fig. S6) [22]. Therefore, it may exhibit a flat-CD effect without or with a small external magnetic field. Its estimated g value is 0.16, which is relatively small for the flat-CD effect but still large compared to the conventional chiral molecular CD effect. This is because its flat bands are derived from the benzene ring of C atoms with small SOC. It is important to note that $Cr_2(C_6O_4Cl_2)_3$ has already been experimentally synthesized [34]. The details of the computational methods are shown in the Supplemental Material [22].

V. FLATBAND DEVICES

Last, we propose two conceptual flatband devices based on the unique topological optoelectronic properties of enantiomorphic FCBs: A topological photodetector and a CP laser.
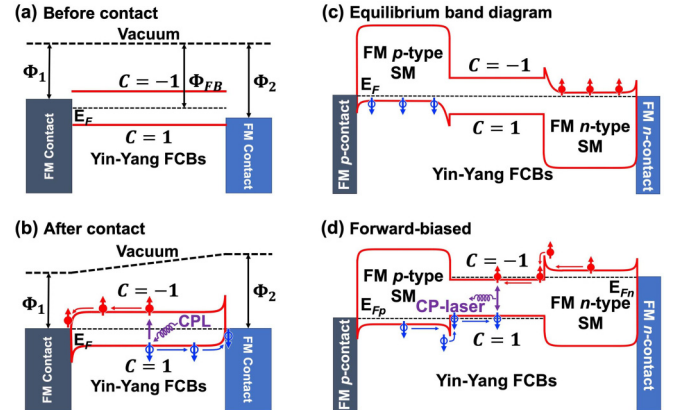

FIG. 6. Schematic band diagrams of two flatband device setups. (a) The band diagrams of the yin-yang FCBs and two ferromagnetic (FM) metal contacts with different work functions $\Phi_{1,2}$ before contact in a photovoltaic cell. The Chern numbers are opposite for yin and yang FCBs. (b) The band diagram after contact. A σ^+ CPL excitation creates a spin-up electron in the top yang FCB and leave behind a spin-down hole in the bottom yin FCB. The electron (hole) flows to the left (right) FM contact with a smaller (larger) work function. (c) The equilibrium band diagram of a spin-polarized double heterostructure made of a FM p contact/FM p-type semiconductor (SM)/yin-yang FCB material/FM n-type SM/FM n contact. The Fermi level E_F is constant across the junction. (d) The band diagram after a forward bias applied to (c) where the spin-up electrons and spin-down holes are injected into yang and yin FCBs, respectively, and the electron-hole recombination emits a CP laser. E_{Fn} (E_{Fp}) represents the quasi-Fermi level of electrons (holes).

Similar to valleytronic devices [35–37] where the topology-triggered chirality-dependent phototransitions between valley bands, such as valley-CD and valley Hall effects, are exploited to achieve various device functions, flatband devices exploit the topology triggered chirality-dependent phototransitions between flat bands, such as flat-CD and FB Hall effects [20]. However, there are some important differences. In flatband devices, first, the photoexcited FB Hall conductivity can be quantized, while the valley Hall conductivity cannot, as explained before [20]. One can take advantage of quantization to build robust topological photodetectors in a photovoltaic cell, as illustrated in Figs. 6(a) and 6(b). Second, the FCBs in the whole Brillouin zone contribute to the CD effect in one chirality without the need to select one of the two sets of valleys whose CD effects would cancel out each other [12,19]. This will enable us to build CP lasers in a heterojunction diode, as illustrated in Figs. 6(c) and 6(d).

In Figs. 6(a) and 6(b), a yin-yang FCB material is placed in contact with two ferromagnetic metal contacts with different work functions with $\Phi_1 < \Phi_{FB} < \Phi_2$. The system works effectively like a photovoltaic cell. After contact, as the Fermi level is aligned, an electrostatic potential is built up, as shown in Fig. 6(b). A σ^+ CPL excites a spin-up electron from the valence yin FCB ($C = 1$), leaving behind a spin-down hole, to the conduction yang FCB ($C = -1$). Driven by the electrostatic potential, the electron and hole flow to the left and right ferromagnetic (FM) contacts with smaller and large work functions, respectively. More interestingly, in a four-probe setup, there will be quantized photoexcited transverse Hall conductivity because the system exhibits an excited quantum anomalous Hall effect [20], functioning like a highly sensitive and robust topological CP photodetectors. In the second application, one can construct a solid-state CP laser in a spin-polarized double-heterostructure diode, where the yin-yang FCB material is sandwiched in a FM p contact/FM p-type semiconductor (SM)/yin-yang FCB material/FM n-type SM/FM n-contact heterojunction. Figure 6(c) shows the equilibrium band diagram of the diode, where electrons and holes are confined in the FM n- and p-type SM layers, respectively. By applying a forward bias [Fig. 6(d)], electrons and holes are injected into the highly localized dispersionless yang and yin FCBs, respectively, and their recombination radiates a CP laser.

[1] N. Berova, K. Nakanishi, and R. W. Woody, *Circular Dichroism: Principles and Applications* (Wiley, New York, 2000).

[2] L. D. Barron, *Molecular Light Scattering and Optical Activity* (Cambridge University Press, Cambridge, 2009).

[3] A. Rodger and B. Nordén, *Circular Dichroism and Linear Dichroism* (Oxford University Press, New York, 1997), Vol. 1.

[4] S. Sato, A. Yoshii, S. Takahashi, S. Furumi, M. Takeuchi, and H. Isobe, Proc. Natl. Acad. Sci. USA **114**, 13097 (2017).

[5] S. Yang, Z. Liu, S. Hu, A.-Z. Jin, H. Yang, S. Zhang, J. Li, and C. Gu, Nano Lett. **19**, 3432 (2019).

[6] A. Rycerz, J. Tworzydło, and C. Beenakker, Nat. Phys. **3**, 172 (2007).

[7] A. R. Akhmerov and C. W. J. Beenakker, Phys. Rev. Lett. **98**, 157003 (2007).

[8] D. Xiao, W. Yao, and Q. Niu, Phys. Rev. Lett. **99**, 236809 (2007).

[9] W. Yao, D. Xiao, and Q. Niu, Phys. Rev. B **77**, 235406 (2008).

[10] R. Gorbachev, J. Song, G. Yu, A. Kretinin, F. Withers, Y. Cao, A. Mishchenko, I. Grigorieva, K. Novoselov, L. Levitov *et al.*, Science **346**, 448 (2014).

[11] D. Xiao, G.-B. Liu, W. Feng, X. Xu, and W. Yao, Phys. Rev. Lett. **108**, 196802 (2012).

[12] T. Cao, G. Wang, W. Han, H. Ye, C. Zhu, J. Shi, Q. Niu, P. Tan, E. Wang, B. Liu *et al.*, Nat. Commun. **3**, 887 (2012).

[13] W. Feng, Y. Yao, W. Zhu, J. Zhou, W. Yao, and D. Xiao, Phys. Rev. B **86**, 165108 (2012).

[14] J. Qi, X. Li, Q. Niu, and J. Feng, Phys. Rev. B **92**, 121403(R) (2015).

[15] W.-Y. Tong, S.-J. Gong, X. Wan, and C.-G. Duan, Nat. Commun. **7**, 13612 (2016).

[16] N. Singh and U. Schwingenschlögl, Adv. Mater. **29**, 1600970 (2017).

[17] C. Zhao, T. Norden, P. Zhang, P. Zhao, Y. Cheng, F. Sun, J. P. Parry, P. Taheri, J. Wang, Y. Yang *et al.*, Nat. Nanotechnol. **12**, 757 (2017).

[18] H. Beyer, G. Rohde, A. Grubišić Čabo, A. Stange, T. Jacobsen, L. Bignardi, D. Lizzit, P. Lacovig, C. E. Sanders, S. Lizzit, K. Rossnagel, P. Hofmann, and M. Bauer, Phys. Rev. Lett. **123**, 236802 (2019).

[19] Z.-M. Yu, S. Guan, X.-L. Sheng, W. Gao, and S. A. Yang, Phys. Rev. Lett. **124**, 037701 (2020).

[20] Y. Zhou, G. Sethi, H. Liu, and F. Liu, arXiv:1908.03689.

[21] C. L. Kane and E. J. Mele, Phys. Rev. Lett. **95**, 146802 (2005).

[22] See Supplemental Material at http://link.aps.org/supplemental/10.1103/PhysRevB.102.125115 for more details, including Refs. [38–54].

[23] D. J. Thouless, M. Kohmoto, M. P. Nightingale, and M. den Nijs, Phys. Rev. Lett. **49**, 405 (1982).

[24] L. C. Lew Yan Voon and L. R. Ram-Mohan, Phys. Rev. B **47**, 15500 (1993).

[25] M. Graf and P. Vogl, Phys. Rev. B **51**, 4940 (1995).

[26] M. S. Dresselhaus, G. Dresselhaus, and A. Jorio, *Group Theory: Application to the Physics of Condensed Matter* (Springer-Verlag, Berlin, Heidelberg, 2008).

[27] M. Saba, M. D. Turner, K. Mecke, M. Gu, and G. E. Schröder-Turk, Phys. Rev. B **88**, 245116 (2013).

[28] G. F. Koster, J. O. Dimmock, G. Wheeler, and R. G. Satz, *Properties of Thirty-Two Point Groups* (MIT Press, Cambridge, MA, 1963), Vol. 24.

[29] B. A. Bernevig, T. L. Hughes, and S.-C. Zhang, Science **314**, 1757 (2006).

[30] Z. Wang, K.-H. Jin, and F. Liu, Nat. Commun. **7**, 12746 (2016).

[31] T. Kambe, R. Sakamoto, T. Kusamoto, T. Pal, N. Fukui, K. Hoshiko, T. Shimojima, Z. Wang, T. Hirahara, K. Ishizaka *et al.*, J. Am. Chem. Soc. **136**, 14357 (2014).

[32] F. C. de Lima, G. J. Ferreira, and R. H. Miwa, Phys. Rev. B **96**, 115426 (2017).

[33] F. Crasto de Lima, G. Ferreira, and R. Miwa, J. Chem. Phys. **150**, 234701 (2019).

[34] M. E. Ziebel, L. E. Darago, and J. R. Long, J. Am. Chem. Soc. **140**, 3040 (2018).

[35] H. Zeng, J. Dai, W. Yao, D. Xiao, and X. Cui, Nat. Nanotechnol. **7**, 490 (2012).

[36] K. F. Mak, K. He, J. Shan, and T. F. Heinz, Nat. Nanotechnol. **7**, 494 (2012).

[37] J. R. Schaibley, H. Yu, G. Clark, P. Rivera, J. S. Ross, K. L. Seyler, W. Yao, and X. Xu, Nat. Rev. Mater. **1**, 16055 (2016).

[38] H. Yao and S. A. Kivelson, Phys. Rev. Lett. **99**, 247203 (2007).

[39] A. Rüegg, J. Wen, and G. A. Fiete, Phys. Rev. B **81**, 205115 (2010).

[40] J. Wen, A. Rüegg, C.-C. J. Wang, and G. A. Fiete, Phys. Rev. B **82**, 075125 (2010).

[41] M. Chen and S. Wan, J. Phys.: Condens. Matter **24**, 325502 (2012).

[42] W.-C. Chen, R. Liu, Y.-F. Wang, and C.-D. Gong, Phys. Rev. B **86**, 085311 (2012).

[43] C. Wu and S. Das Sarma, Phys. Rev. B **77**, 235107 (2008).

[44] Z. Liu, Z.-F. Wang, J.-W. Mei, Y.-S. Wu, and F. Liu, Phys. Rev. Lett. **110**, 106804 (2013).

[45] M. Zhou, W. Ming, Z. Liu, Z. Wang, P. Li, and F. Liu, Proc. Natl. Acad. Sci. USA **111**, 14378 (2014).

[46] K. Ohgushi, S. Murakami, and N. Nagaosa, Phys. Rev. B **62**, R6065(R) (2000).

[47] H.-M. Guo and M. Franz, Phys. Rev. B **80**, 113102 (2009).

[48] P. E. Blöchl, Phys. Rev. B **50**, 17953 (1994).

[49] G. Kresse and D. Joubert, Phys. Rev. B **59**, 1758 (1999).

[50] J. P. Perdew, K. Burke, and M. Ernzerhof, Phys. Rev. Lett. **77**, 3865 (1996).

[51] G. Kresse and J. Furthmüller, Phys. Rev. B **54**, 11169 (1996).

[52] D. Hobbs, G. Kresse, and J. Hafner, Phys. Rev. B **62**, 11556 (2000).

[53] S. Grimme, J. Comput. Chem. **27**, 1787 (2006).

[54] T. Bucko, J. Hafner, S. Lebegue, and J. G. Angyán, J. Phys. Chem. A **114**, 11814 (2010).